HHS Public Access

Author manuscript

Langmuir. Author manuscript; available in PMC 2019 May 09.

Published in final edited form as:

Langmuir. 2018 June 05; 34(22): 6454–6461. doi:10.1021/acs.langmuir.7b03741.

Nanoparticle Wettability Influences Nanoparticle–Phospholipid Interactions

Nagarjun V. Konduru[†,‡], **Flavia Damiani**[†], **Svetla Stoilova-McPhie**[§], **Jason S. Tresback**[§], **Georgios Pyrgiotakis**[†,‡], **Thomas C. Donaghey**[†,‡], **Philip Demokritou**[†,‡], **Joseph D. Brain**[†,‡], and **Ramon M. Molina**[*,†,‡]

[†] Molecular and Integrative Physiological Sciences Program, Department of Environmental Health, Harvard T.H. Chan School of Public Health, 665 Huntington Avenue, Boston, Massachusetts 02115, United States

[‡] Center for Nanotechnology and Nanotoxicology, Harvard T.H. Chan School of Public Health, 665 Huntington Avenue, Boston, Massachusetts 02115, United States

[§] Center for Nanoscale Systems, Faculty of Art and Sciences, Harvard University, 11 Oxford Street, Cambridge, Massachusetts 02138, United States

Abstract

We explored the influence of nanoparticle (NP) surface charge and hydrophobicity on NP—biomolecule interactions by measuring the composition of adsorbed phospholipids on four NPs, namely, positively charged CeO_2 and ZnO and negatively charged $BaSO_4$ and silica-coated CeO_2, after exposure to bronchoalveolar lavage fluid (BALf) obtained from rats, and to a mixture of neutral dipalmitoyl phosphatidylcholine (DPPC) and negatively charged dipalmitoyl phosphatidic acid (DPPA). The resulting NP—lipid interactions were examined by cryogenic transmission electron microscopy (cryo-TEM) and atomic force microscopy (AFM). Our data show that the amount of adsorbed lipids on NPs after incubation in BALf and the DPPC/DPPA mixture was higher in CeO_2 than in the other NPs, qualitatively consistent with their relative hydrophobicity. The relative concentrations of specific adsorbed phospholipids on NP surfaces were different from their relative concentrations in the BALf. Sphingomyelin was not detected in the extracted lipids from the NPs despite its >20% concentration in the BALf. AFM showed that the more hydrophobic CeO_2 NPs tended to be located inside lipid vesicles, whereas less hydrophobic $BaSO_4$ NPs appeared to be outside. In addition, cryo-TEM analysis showed that CeO_2 NPs were associated with the formation of multilamellar lipid bilayers, whereas $BaSO_4$ NPs with unilamellar lipid bilayers. These data suggest that the NP surface hydrophobicity predominantly controls the amounts and types of lipids adsorbed, as well as the nature of their interaction with phospholipids.

Graphical Abstract

[*]**Corresponding Author:** rmolina@hsph.harvard.edu. Phone: 617-432-2311.

The authors declare no competing financial interest.

ASSOCIATED CONTENT

Supporting Information

The Supporting Information is available free of charge on the ACS Publications website at DOI: 10.1021/acs.langmuir.7b03741.

Online supplement is available (PDF)

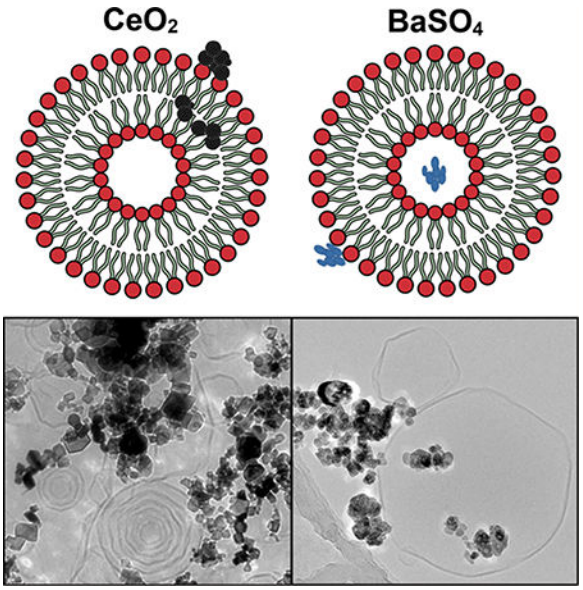

INTRODUCTION

When introduced into a biological milieu, nanoparticles (NPs) encounter a mixture of biomolecules (e.g., proteins, lipids, sugars, ions, and enzymes). Some may spontaneously adsorb onto the NP surface, forming the NP corona.[1] These interactions are often dynamic, including sequential adsorption and desorption cycles.[2] When inhaled, NPs encounter these biomolecules including pulmonary surfactants on lung surfaces. Events that occur even before the NPs deposit in lungs, such as adsorption of air contaminants or NP aggregation, can also affect corona formation. The lungs have two major components: the conducting airways and the gas exchange region, containing the alveoli. Depending on particle size, lung anatomy, and breathing patterns, inhaled NPs and larger particles, may deposit in the airways or alveoli.[3,4] When deposited in the parenchyma, particles first encounter the pulmonary surfactant layer, which resides on top of the alveolar lining fluid.[5] The intrinsic physicochemical characteristics of NPs, such as size, hydrophobicity, and surface charge, and the extrinsic properties of the suspending medium, such as protein and phospholipid (PL) concentrations, influence NP-biomolecule interactions, corona formation, and subsequent NP biological effects and kinetics.[6–8] Studying these interactions and their relative importance for different categories of NPs is a major challenge in the field of nanotoxicology.[9]

A pulmonary surfactant is composed of 85–90 w/w % PLs; the remaining 10 w/w % is proteins.[10] The saturated lipid dipalmitoyl phosphatidylcholine (DPPC) is the most abundant, followed by monoenoic phosphatidylcholine, cholesterol, and anionic PLs.[11] Structurally, DPPC contains a hydrophilic zwitterionic trimethyl ammonium and acidic phosphate head and two hydrophobic long-chain fatty acid tails esterified to the glycerol. The DPPC-enriched lung lining fluid functions to prevent the collapse of alveoli as exhalation reduces the alveolar diameter by producing a near-zero surface tension. Monolayers of DPPC endure a high surface pressure (or low surface tension) for a

considerable time without collapsing.[12–14] Predominantly, hydrogen bonding and electrostatic interactions control the interactions between DPPC and NP surfaces.[15] Although protein corona formation on NPs has been studied,[16] PL-NP interactions or formation of corona PL is less explored. A recent study investigated the influence of hydrophobic and hydrophilic NPs on the mechanical properties of the DPPC monolayer. It was found that hydrophilic halloysite and bentonite NPs induced a concentration-dependent impairment of DPPC's ability to attain high surface pressures on interfacial compression, suggesting the possibility of reduced physiological function of the lung surfactant.[17]

Few studies emphasize the role of surfactant PLs in lung macrophage-mediated particle uptake. Ruge et al. demonstrated that surfactant lipids that modulate protein-mediated particle agglomeration of NPs might play an important role in the clearance of NPs by alveolar macrophages.[18] Kapralov et al. reported that coating single-wall carbon nanotubes (SWCNTs) with surfactant PLs significantly enhanced their uptake in a RAW 264.7 macrophage cell line.[19] Furthermore, coating with deficient PLs in either phosphatidylglycerol (PG) or phosphatidylserine (PS) led to a significant reduction in macrophage phagocytosis of the coated SWCNTs. We also showed that coating of SWCNTs with PS and not PC promoted their uptake by professional phagocytes.[20] Because alveolar macrophages play a critical role in NP-induced inflammation, oxidative stress, and innate immune function, it is possible that the formation of the NP lipid corona may influence NP fate and biological effects.[21]

Recently, Raesch et al. showed that magnetite NPs with different surface functionalizations (PEG-, PLGA-, and lipid—NP) acquired different protein corona compositions but had similar classes of PLs.[22] Formation of "corona-like" supported bilayers around model silica NPs after incubation in surfactant mixtures such as CUROSURF[23] and SURVANTA[24] has been studied. Similarly, the interactions of inorganic nanomaterials with model PC bilayers have been studied.[25] However, there is currently little information about the nature of PL—NP interactions in the lungs, particularly for industrially relevant NPs. Obtaining such information will require both in vitro and in vivo experiments to quantify PL corona formation under a variety of conditions as well as mechanism-based models. We hypothesize that the NP surface characteristics influence the interactions of liposome-like structures present in the bronchoalveolar lavage fluid (BALf) with NPs, their interactions with the NP surface, and the subsequent formation of "corona-like" bilayers around the NPs.

In this study, we performed quantitative and qualitative analyses of the different PL species adsorbing onto the surface of four different engineered NPs after exposure to rat BALf. In addition, we also characterized the PL-NP interactions in a more controlled formulation composed of a DPPC/dipalmitoyl phosphatidic acid (DPPA) mixture using cryogenic transmission electron microscopy (cryo-TEM) and atomic force microscopy (AFM). To our knowledge, this is the first study examining the interactions of engineered NPs with rat surfactants obtained by lung lavage using cryo-TEM. We believe that the data from this study using cryo-TEM and AFM techniques will provide important insights about the nature of interactions between engineered NPs and PLs.

MATERIALS AND METHODS

Synthesis and Characterization of NPs

Uncoated CeO_2, silica-coated CeO_2, and ZnO NPs were synthesized by flame spray pyrolysis using the Versatile Engineered Nanomaterial Generation System (VENGES) at Harvard University.[26] Detailed physicochemical and morphological characterization of these NPs was reported earlier.[27,28] BaSO4 NPs (NM-220) were obtained from BASF SE (Ludwigshafen, Germany). This is a reference material for the Nanomaterial Testing Sponsorship Program of the Organization for Economic Cooperation and Development (OECD). Characterization of the NM-220 batch was previously published.[29]

Measurement of NP Surface Hydrophobicity

We used the Rose Bengal assay to determine the surface hydrophobicity of test NPs according to published protocols.[30,31] The partitioning quotient (PQ) was determined as the ratio of RB bound to the NP surface to free RB in the liquid phase ($PQ = RB_{bound}/RB_{free}$). The PQ values were plotted as a function of NP surface area and fit by a straight line using SAS statistical software (SAS Institute, Inc., Cary, NC). The slope was taken to represent the relative surface hydrophobicity, with increasing slope indicating increasing surface hydrophobicity.[30]

Hydrodynamic Diameter and Zeta Potential

CeO_2, silica-coated CeO_2, BaSO4, and ZnO NPs were suspended in distilled water at specified concentrations and were sonicated in conical polyethylene tubes. A critical dispersion sonication energy (DSE_{cr}) to achieve the smallest particle agglomerate size was used, as previously reported.[28,32] The suspensions were sonicated at 242 J/mL (20 min/mL at 0.2 W power output) in a cup sonicator fitted on Sonifier S-450A (Branson Ultrasonics, Danbury, CT). The sample tubes were immersed in running cold water to minimize heating of the particles during sonication. The hydrodynamic diameter (D_H) and zeta potential (ζ) of each aggregate suspension were measured using Zetasizer Nano ZS (Malvern Instruments, Worcestershire, UK).

Collection of BALf

The protocols used in this study were approved by the Harvard Medical Area Animal Care and Use Committee. Twelve male Wistar Han rats (8 weeks old) were obtained from Charles River Laboratories (Wilmington, MA) and were housed in standard microisolator cages under controlled conditions of temperature, humidity, and light at the Harvard Center for Comparative Medicine. Rats were euthanized and exsanguinated via the abdominal aorta under isoflurane anesthesia. The trachea was exposed and cannulated. The lungs were then lavaged with 5 mL of Ca^{2+}- and Mg^{2+}-free 0.9% sterile PBS by introducing the same solution in and out of the lungs three times to obtain representative samples of BALf. A cell-free BAL supernatant was obtained after centrifugation (350*g* at 4 °C for 10 min). BALf samples from three rats were pooled for each NP incubation.

PL Extraction and Analyses

Sonicated NP suspensions were added to BALf or DPPC/DPPA lipid mixture. In the case of DPPC/DPPA, the NP—lipid mixture was further sonicated for 30 min prior to incubation. After incubation in BALf and in DPPC/DPPA lipid mixture, the NP suspensions were centrifuged (14 500*g* for 10 min). The NP pellets containing the adsorbed PLs were suspended in 600 μL of deionized (DI) water and transferred into a glass tube. Two milliliters of 1:2 chloroform/methanol solution (v/v) were added and vortexed. Then, 600 μL of saline was added and vortexed. Finally, 600 μL of chloroform was added, and the resulting suspension was spun at 3000*g* for 10 min. Without disturbing the two phases, the lower phase containing PLs was collected into separate glass vials and the samples were dried in nitrogen gas.

The dried PL samples were reconstituted with 0.5 mL of 1:1 chloroform/methanol (v/v). To extract PLs from BALf, 1 mL of BALf was removed with 2 mL of 1:1 (v/v) chloroform/methanol. The lower layer was diluted to a final volume of 10 mL in 1:1 (v/v) chloroform/methanol. Analysis of extracted PL from BALf-incubated NPs was performed using an Acquity UPLC/AB Sciex 5500 tandem quadrupole mass spectrometer.[19] An aliquot of each sample was diluted 1:10 into an internal standard solution (ISTD) containing 17:1 lyso and 17:0—30:1 PL of phosphatidylethanolamine (PE), phosphatidylinositol (PI), PG, PS, phosphatidic acid (PA), and sphingomyelin (SM). Samples for PC were diluted 1:100 in the same ISTD mixture. The samples were injected under a reverse phase gradient onto an Agilent Eclipse XDB-C8 column of 50 × 4.6 (i.d.) mm, 1.8 μM. The mass spectrometer was programmed for a multiple reaction monitoring for the molecular species of each PL class.[19] Each molecular species identified above a 10:1 signal to noise was quantified against the response of the class relevant internal standard of known concentration.

NPs for the DPPC/DPPA experiments were sonicated with 100 μg DPPC/50 μg DPPA at a NP/PL ratio of 6:1 (five cycles 30 s) in a cold water bath sonicator. Then, the NP-DPPC/DPPA suspension was incubated at 37 °C for 30 min. The NPs were then centrifuged at 14 500*g* for 30 min, and the resulting pellet was washed three times with 25 mM HEPES, pH 7.4. After each wash, the samples were centrifuged at 14 500*g* for 30 min at 4 °C. PLs from coated NPs were extracted using the Folch procedure.[33] Lipid phosphorus content was determined using a modification of the method for microdetection (1–10 nmol).[34] Aliquots of lipid extracts were transferred into test tubes, and the solvent was evaporated to dryness under a stream of oxygen-free dry N_2. Fifty microliters of 70% (w/w) $HClO_4$ was added to the dried samples, which were then incubated for 20 min at 170–180 °C. After cooling, 0.4 mL of H_2O was added to each tube followed in succession by 2 mL of sodium molybdate-malachite green reagent solution [1:3 (v/v) 4.2% (w/v) sodium molybdate in 5.0 M HCl-0.2% (w/v) aqueous malachite green] and 80 μL of 1.5% (v/v) Tween 20. The tubes were shaken immediately to stabilize the developed color, which was measured at 660 nm in a SpectraMax M5 spectrophotometer (Molecular Devices, Sunnyvale, CA).

Cryogenic Transmission Electron Microscopy

Cerium oxide and $BaSO_4$ NPs were incubated in BALf or in a 2:1 mixture of DPPC and DPPA as described earlier. Holey carbon grids for electron microscopy (Quantifoil 2 × 1,

Electron Microscopy Sciences, Hatfield, PA) were hydrophilized for 25 s. Five microliters of the NP suspension was deposited on the grids and incubated for 1 min. The grid was mounted on a semiautomatic Cryoplunge—Gatan CP3 (Gatan, Inc., Pleasanton, CA) and plunged in liquid ethane, cooled down by liquid nitrogen to preserve the fully hydrated structures in amorphous ice. The grids were then transferred under liquid nitrogen in a Tecnai Arctica operated at 200 kV equipped with a field emission gun and autoloader (Thermo Fisher, Hillsboro, OR). Digital images were collected at low-dose conditions (~24 $e^{-}/Å^2$ s) at 23 500× and 39 000× magnification with a 4096 × 4096 pixel charge-coupled device camera at 2.5 and 3.83 Å/pixels resolution, respectively.

Atomic Force Microscopy

AFM analyses of the same NP suspensions were performed using an MFP3d-BIO instrument (Asylum Research, Santa Barbara, CA) by drop-casting and spincasting the NP-DPPC/DPPA aqueous suspension on freshly cleaved mica (V1 grade, Ted Pella, Redding, CA). Imaging was performed in a noncontact, ac/tapping mode in air using soft (2 N/m) cantilevers with a 7:1 aspect ratio silicon tip (AC240BSA, Asylum Research, Santa Barbara, CA). The height images were masked and flattened using instrument software.

RESULTS AND DISCUSSION

NP Characteristics

The physicochemical characteristics of the NPs used in this study are shown in Figure 1 and Table 1. Values shown were obtained after the NPs were suspended in DI water and sonicated. Each NP suspension was then examined by TEM. The shapes and morphology of each NP are shown in Figure 1. The zeta-potential measurements for CeO_2, Si-CeO_2, $BaSO_4$, and ZnO NPs in DI water were +34.5 ± 3.2, −26.8 ± 0.3, −18.5 ± 1.9, and +23 ± 0.4 mV, respectively. The hydrodynamic sizes of NPs measured in DI water using dynamic light scattering (DLS) showed that all four NP types formed agglomerates. Among the four NPs, ZnO showed a greater propensity to form larger agglomerates in DI water (221 nm), followed by Si-CeO_2 (208 nm), $BaSO_4$ (144 nm), and CeO_2 (136 nm). The rod shape of ZnO NPs may have contributed to higher mean DLS agglomerate size compared to the other cubical and spherical NPs. The NPs were incubated in cell-free BALf for 30 min at 37 °C. After incubation, the zeta potentials changed to −23.2 ± 1.4 mV (CeO_2), −16.7 ± 1.3 mV (Si-CeO_2), −34.5 ± 2.7 mV ($BaSO_4$), and −20.8 ± 1.7 mV (ZnO). After exposure to BALf, there were increases in agglomerate size in all NPs (Table 1). The relative increases were on the order of ZnO > CeO_2 > $BaSO_4$ > Si-CeO_2 NPs.

Using the Rose Bengal partitioning assay on the four dry powders, we characterized the relative surface hydrophobicity of the four NPs. The linear relationships between NP surface areas and PQ were plotted. The slopes of the linear regression lines are proportional to the relative hydrophobicities of NPs. The slopes of PQ for each NP were compared using SAS statistical software (SAS Institute, Inc. Cary, NC). We found that the relative surface hydrophobicity was on the order of CeO_2 > ZnO = $BaSO_4$ > Si-CeO_2 NPs (Figure 2).

The surface chemistry of NPs influences their agglomeration and the formation of protein coronas around them.[16,35] The interactions between lipids and surfaces of NPs are complex and are an active area of research. The NP-lipid interactions can be mediated by van der Waals, double layers, hydration, hydrophobic, thermal undulation, and protrusion forces.[36,37] In our experiments, we could not determine whether NPs aggregate first and then interact with PLs or whether PLs interact with individual particles which then aggregate. Perhaps both processes take place in parallel. Nevertheless, both possible processes can lower the surface energy of NPs.[7,35] It is important to note that although lung surfactant contains different PLs, it also contains proteins (10%). Another mechanism that might contribute to increased agglomerate size includes lipid membrane fusion. This is a natural process of many biological events such as fertilization, viral membrane fusion with host cells, and exosome fusion to cell membranes.[38] In some instances, proteins aid in such fusion processes to form larger structures by acting as fusogenic agents. In other situations, the transition from the lamellar bilayer phase to inverted hexagonal phase has been proposed as a step toward mixing of the outer bilayer of lipids to promote fusion.[39,40]

Adsorption of PLs from BALf on NPs

The composition of PLs extracted from NPs after incubation in BALf for 30 min at 37 °C was analyzed by chloroform/methanol extraction followed by the liquid chromatography—mass spectrometry analysis of the PLs. The amount of PL bound per unit surface area (mg/m^2) had the following order: CeO_2 (1.76 ± 0.06) > Si—CeO_2 (1.19 ± 0.06) = ZnO (1.14 ± 0.02) > $BaSO_4$ (0.90 ± 0.10) NPs (Figure 3a). Because these surface area calculations were based on Brunauer—Emmett—Teller analyses of dry powder, the influence of NP agglomeration in BALf on specific surface areas was not measured.

The quantitative analyses of major PLs bound onto NPs are shown in Figure 3b and Table 2. Phosphatidylcholine (PC) comprises more than 90% of the total PL fraction bound to NPs (Figure 3, Table S1, Online Supporting Information). At least 40 different species of PC were present (Table S1, Online Supporting Information). Of these, the seven most abundant either saturated or monounsaturated fatty acid chains belonged to C32:0; C32:1; C34:2; C34:1; C34:0; C30:1; and C16:0, where the first number is the total number of carbons in the two tails of the lipids and the second is the number of double bonds. Among the PC species, DPPC, which is C32:0, the major surface-active component of lung surfactant, was the most abundant PL species binding to all four NPs. Interestingly, the C18:2 PC species bound only to ZnO NPs. None were found in the other three NPs. Similarly, the PL C30:0e species (with “e” standing for ether) was found on CeO_2 and Si—CeO_2 but was absent from both ZnO and $BaSO_4$ NPs.

PA (C38:5), an anionic PL and a precursor PL in the biosynthesis of lung surfactant, was the next most abundant PL class in all four NPs. A larger mass percentage of adsorbed PA species was in CeO_2 (5.7%) than in $BaSO_4$ (4.2%), Si—CeO_2 (4.4%), and ZnO NPs (1.6%). Interestingly, the highest percentage of another anionic PL, PS, was measured in ZnO NPs, followed by $BaSO_4$ and then Si—CeO_2. The levels of PS were lowest in the extracted PLs from CeO_2 NPs despite their positively charged surfaces. The relative abundances of PA, phosphatidylinositol (PI), and PG species adsorbed onto NP surfaces were found to be

different from the concentrations in native rat BALf in which the particles had been incubated (Table 3), indicating preferential adsorption of some of the PL species. Surprisingly, despite high SM levels in rat lung BALf (22.4%), no detectable SM was found adsorbed on the NPs (Table S1, Online Supporting Information). Although PA is a minor PL in the normal lung lining fluid (only 0.15% of the total PL pool), it constituted 1.6—5.7% on the NP surfaces (Table 3). In contrast, 0.8—1% of the NP-bound lipid was composed of PI, much lower than the 2.87% of the total PL pool.

Comparison of Adsorption of PLs on NPs: BALf Versus DPPC/DPPA Mixture

We also studied adsorption onto NPs of a simpler lipid mixture than that found in BALf, namely, a 2:1 mixture of DPPC and DPPA lipids. The lipid densities measured on the NP surfaces were 0.56 ± 0.01, 0.35 ± 0.02, 0.35 ± 0.02, and 0.34 ± 0.02 mg/m^2 for CeO_2, Si—CeO_2, $BaSO_4$, and ZnO, respectively.

Our results from both the DPPC/DPPA mixture and from the BALf suggest that the total surface densities of the PLs bound to the NP depend mainly on the NP hydrophobicity. The lipid density on CeO_2 NPs is significantly higher than the lipid densities of the other NPs, as seen in Figure 3 for the BALf extracts and for DPPC/DPPA mixtures. From the studies with BALf in Figure 3a, lipid adsorption onto $BaSO_4$ is slightly lower than that on ZnO and Si-CeO_2. There were no significant differences in extracted lipids among Si-CeO_2, $BaSO_4$, and ZnO NP postincubation in the DPPC/DPPA mixture. The slope of the lines in the Rose Bengal assay in Figure 2 shows Si-CeO_2 to be slightly less hydrophobic than the other NPs, but this difference did not affect lipid adsorption. Neither the sign nor the magnitude of the surface charge on the NPs correlates with lipid adsorption. In regard to adsorption from BALf, similar adsorbed amounts were found on ZnO as on Si-CeO_2, despite having opposite surface charge. The least negatively charged NP, $BaSO_4$, (zeta potential −18.5 ± 1.9 mV) adsorbs slightly less lipid than does a more negatively charged NP, Si-CeO_2 (zeta potential −26.8 ± 0.3 mV), despite the greater repulsion of negatively charged lipids that one might expect when the NP becomes more negatively charged. Thus, although NP charge, size, shape, and other factors may influence PL-NP interactions, experimentally the only significant influence that is clearly demonstrated in our data is NP hydrophobicity.

Interaction of NPs with PLs in BALf

To examine the interactions between PLs and NPs, using cryo-TEM, we examined samples of NPs incubated in either BALf or a DPPC/DPPA mixture. We selected CeO_2 and $BaSO_4$ as model NPs because these have different surface hydrophobicity and opposite surface charge. As BALf is a complex mixture comprising both PLs and proteins, we also studied the PL-NP interactions using model lipid vesicles prepared from a mixture of DPPC and DPPA PLs. DPPC is a major PL component of the lung surfactant. These are also the predominant lipid species interacting with NPs we observed after incubation in BALf. Although DPPA is not present in the lung surfactant, PAs are present. We included DPPA because its tail groups are identical to those of DPPC. Figure S1 shows a cryo-TEM image of BALf, showing large sheets of lipid bilayers in micron sizes covering multiple holes of the grid. Cryo-TEM analysis showed agglomerates of CeO_2 (Figure 4a) and $BaSO_4$ (Figure 4b) NPs interacting with these large liposome-like structures present in the BALf. On the basis of cryo-TEM

images, we could not determine exactly how the lipid structures interact with individual or agglomerated NPs. There was no clear evidence of “corona-like” lipid bilayers surrounding the NPs. We observed lipid bilayer vesicles (~100–200 and >500 nm) interacting with both $BaSO_4$ and CeO_2 NPs (Figure 4). Importantly, we observed that both NPs formed larger agglomerates after incubation in BALf than when suspended in distilled water (Figure 1). Furthermore, the particle agglomerates of CeO_2 were larger compared to $BaSO_4$ NPs (Figure 4). These observations are also supported by DLS measurements of hydrodynamic diameters of NPs in distilled water and after incubation in BALf (Table 1). Although cryo-TEM could not determine whether NPs were encapsulated or not in lipid vesicles, it was apparent that agglomerates of both NPs were interacting with lipid vesicles.

Interaction of NPs with DPPC/DPPA PLs

We also examined the NP interactions with a simpler PL mixture of DPPC/DPPA. These two PLs exhibit different charges (neutral and anionic). We hypothesized that their interactions with NPs with opposite zeta potentials would be different. The cryo-TEM analysis of CeO_2 (Figure 5a,b) and $BaSO_4$ (Figure 5c,d) NPs incubated in DPPC/DPPA lipid mixtures showed agglomerates of NPs interacting with PL vesicles with polyhedral shapes. Interestingly, we observed CeO_2 NPs interacting with concentrically enclosed multilamellar PL structures of variable sizes (Figure 5a). These onion layer-like vesicular structures were rarely present in the $BaSO_4$ NPs. Instead, predominantly unilamellar PL vesicles were associated with the $BaSO_4$ NPs (Figure 5c). Unilamellar PL vesicles consisting of a single lipid bilayer synthesized in aqueous solutions such as ultrapure water contain a large aqueous core, and therefore, preferentially encapsulate hydrophilic molecules.[41] Conversely, multilamellar PL vesicles, with lipid bilayers arranged concentrically like in an onion-skin, have high lipid content, which allows them to passively entrap lipophilic molecules.[41] Our cryo-TEM findings show that the $BaSO_4$ NPs were associated with the unilamellar PL vesicles and that the NP clusters displayed no direct interaction with the lipid bilayers (Figure 5c). Interestingly, $BaSO_4$ NPs that were present in close proximity to the vesicles were seen interacting with the bilayers (Figure 5d). On the other hand, intact vesicles were seen interacting with CeO_2 NP agglomerates. There was no evidence of wrapping of lipid bilayers around the CeO_2 NPs. NPs decorating the surfaces of unilamellar and multilamellar PL vesicles were observed. In a similar study by Wang and Liu, adsorption of 1,2-dioleoyl-*sn*-glycero-3-phosphocholine liposomes onto the surfaces of TiO_2, ZnO, and Fe_3O_4 NPs was observed with no evidence of bilayer formation around these NPs.[25] In the same study, the formation of bilayers wrapping around the NP surface was only observed in SiO_2 NPs. The wrapping of lipid bilayers around SiO_2 NPs was attributed to the presence of a thin water layer between silica and the liposome surfaces. This minimizes the steric hindrance and allows lipid membrane fusion and formation of supported bilayers. Our results show that unilamellar and multilamellar vesicles exhibited a polyhedral rather than a spherical shape. Similar findings by other groups have ascribed this behavior of PLs to their existence in a gel phase under experimental temperatures used.[42]

To verify whether the particle agglomerates were encapsulated within or interacting on vesicle surfaces, we performed AFM analyses on the $BaSO_4$ and CeO_2 NPs incubated in DPPC/DPPA lipids. The height images indicate that the single lipid bilayers are 5–6 nm

above the mica (Figure 6a). The CeO_2 NPs agglomerated into larger clusters protruding up to 250 nm above the lipid bilayers. These stack up around the NP clusters with five or more lipid bilayer sheets assembled around and between the NPs. There is also evidence of the CeO_2 NPs embedded in the lipid bilayer, as indicated by the line profile where the particles protrude 70–80 nm above the bilayers (Figure 6b,c).

Some of the $BaSO_4$ NPs formed smaller agglomerates protruding 50–60 nm above the lipid bilayers, with particle diameters in the range of 10–30 nm (Figure 6e). There was also evidence of a single $BaSO_4$ NP embedded in the lipid bilayer shown at the end of the line profile in Figure 6e and 6f, where the particle protrudes 15 nm above the 5 nm bilayer. On the basis of AFM topography, it was unclear whether the NPs were fully encapsulated within vesicles. However, there is significant incorporation of $BaSO_4$ NPs within the lipid bilayers.

Furthermore, the phase contrast imaging for CeO_2 revealed small phase changes between the lipid bilayer and the particle area (Figure S2b, Online Supporting Information). This suggests that the materials under the AFM tip did not change, indicating that the particles are either inside or on top of the bilayer. If the particles were under the bilayer, we expected that these should also be present on top, without any preferential partition. On the contrary, the $BaSO_4$ had very strong phase shifts from the bilayers to the particle region, indicating that the $BaSO_4$ particles were sitting on top of the bilayer (Figure S2d, Online Supporting Information). Although these suggest that CeO_2 NPs were inside the bilayer, it is unclear whether the NPs are fully encapsulated within vesicles.

Another important phenomenon confirmed by both cryo- TEM and AFM is that the CeO_2 NPs appeared to promote the creation of 3–4 stacked bilayers, whereas the $BaSO_4$ NPs tended to create single lipid bilayer structures. The mechanisms for these observations are unknown. It can be hypothesized that the particle size and wettability can influence the micelle formation and surfactant interactions,[43] as well as surface charge and the particle material characteristics.[44]

CONCLUSIONS

We measured the compositions of extracted PLs from four NPs after incubation in pooled rat BALf and in 2:1 mixtures of DPPC and DPPA The compositions of extracted PLs from positively charged CeO_2 and ZnO and negatively charged silica-coated CeO_2 and $BaSO_4$ NPs differed significantly. The hydrophobic CeO_2 NPs adsorbed the most lipids, whereas the other three NPs adsorbed lower amounts despite differences in the surface charges. The relative amounts of PLs that bind to NPs were not directly proportional to the amounts in the BAL fluid, indicating preferential adsorption of certain PL species. The AFM examination showed that the more hydrophobic CeO_2 NPs tended to be partitioned inside lipid vesicles, whereas less hydrophobic $BaSO_4$ NPs appeared to be outside lipid bilayers. Additionally, cryo-TEM analysis showed that CeO_2 NPs were associated with the formation of multilamellar stacked lipid bilayers, whereas $BaSO_4$ NPs with unilamellar lipid bilayers. These data suggest that NP surface hydrophobicity predominantly controls the amounts and types of lipids adsorbed, as well as the nature of their interaction with PLs. Further investigations are needed to improve our understanding of the consequences of lung

surfactant PL-NP interactions in the lungs. Future studies exploring the selectivity of NPs toward adsorption of specific PL components of the lung surfactant are also warranted. Especially, we need to explore how these interactions affect in vivo biokinetics and biological responses.

Supplementary Material

Refer to Web version on PubMed Central for supplementary material.

ACKNOWLEDGMENTS

This work was supported by the National Institutes of Environmental Health Sciences (NIH-P30ES000002, K99ES025813, and 1U24ES026946). Parts of this study were performed at the Harvard University Center for Nanoscale Systems (CNS), a member of the National Nanotechnology Coordinated Infrastructure Network (NNCI), which is supported by the National Science Foundation under NSF award no. 1541959. The authors also gratefully acknowledge the advice of Dr. Yi Zuo of University of Hawaii on hydrophobicity measurements and Melissa Curran for editorial advice.

REFERENCES

(1). Monopoli MP; Åberg C; Salvati A; Dawson KA Biomolecular coronas provide the biological identity of nanosized materials. Nat. Nanotechnol 2012, 7, 779–786. [PubMed: 23212421]

(2). Monopoli MP; Walczyk D; Campbell A; Elia G; Lynch I; Bombelli FB; Dawson KA Physical-chemical aspects of protein corona: relevance to in vitro and in vivo biological impacts of nanoparticles. J. Am. Chem. Soc 2011, 133, 2525–2534. [PubMed: 21288025]

(3). Brain JD; Valberg PA Deposition of aerosol in the respiratory tract. Am. Rev. Respir. Dis 1979, 120, 1325–1373. [PubMed: 391112]

(4). Buzea C; Pacheco II; Robbie K Nanomaterials and nanoparticles: sources and toxicity. Biointerphases 2007, 2, MR17–MR71. [PubMed: 20419892]

(5). Bastacky J; Lee CY; Goerke J; Koushafar H; Yager D; Kenaga L; Speed TP; Chen Y; Clements JA Alveolar lining layer is thin and continuous: low-temperature scanning electron microscopy of rat lung. J. Appl. Physiol 1995, 79, 1615–1628. [PubMed: 8594022]

(6). Lundqvist M; Stigler J; Elia G; Lynch I; Cedervall T; Dawson KA Nanoparticle size and surface properties determine the protein corona with possible implications for biological impacts. Proc. Natl. Acad. Sci. U.S.A 2008, 105, 14265–14270. [PubMed: 18809927]

(7). Tsuda A; Konduru NV The role of natural processes and surface energy of inhaled engineered nanoparticles on aggregation and corona formation. NanoImpact 2016, 2, 38–44. [PubMed: 29202111]

(8). Pyrgiotakis G; Blattmann CO; Demokritou P Real-time nanoparticle-cell interactions in physiological media by atomic force microscopy. ACS Sustain. Chem. Eng 2014, 2, 1681–1690. [PubMed: 25068097]

(9). Grassian VH; Haes AJ; Mudunkotuwa IA; Demokritou P; Kane AB; Murphy CJ; Hutchison JE; Isaacs JA; Jun Y-S; Karn B; Khondaker SI; Larsen SC; Lau BLT; Pettibone JM; Sadik OA; Saleh NB; Teague C NanoEHS-defining fundamental science needs: no easy feat when the simple itself is complex. Environ. Sci.: Nano 2016, 3, 15–27.

(10). Goerke J Pulmonary surfactant: functions and molecular composition. Biochim. Biophys. Acta, Mol. Basis Dis 1998, 1408, 79–89.

(11). Clements JA; Avery ME Lung surfactant and neonatal respiratory distress syndrome. Am. J. Respir. Crit. Care Med 1998, 157, S59–S66. [PubMed: 9563762]

(12). Goerke J; Gonzales J Temperature dependence of dipalmitoyl phosphatidylcholine monolayer stability. J. Appl. Physiol.: Respir., Environ. Exercise Physiol 1981, 51, 1108–1114.

(13). Leo BF; Chen S; Kyo Y; Herpoldt K-L; Terrill NJ; Dunlop IE; McPhail DS; Shaffer MS; Schwander S; Gow A; Zhang J; Chung KF; Tetley TD; Porter AE; Ryan MP The stability of

silver nanoparticles in a model of pulmonary surfactant. Environ. Sci. Technol 2013, 47, 11232–11240. [PubMed: 23988335]

(14). Zuo YY; Possmayer F How does pulmonary surfactant reduce surface tension to very low values? J. Appl. Physiol 2007, 102, 1733–1734. [PubMed: 17303712]

(15). Guzmán E; Liggieri L; Santini E; Ferrari M; Ravera F Effect of hydrophilic and hydrophobic nanoparticles on the surface pressure response of dppc monolayers. J. Phys. Chem. C 2011, 115, 21715–21722.

(16). Konduru NV; Molina RM; Swami A; Damiani F; Pyrgiotakis G; Lin P; Andreozzi P; Donaghey TC; Demokritou P; Krol S; Kreyling W; Brain JD Protein corona: implic/ations for nanoparticle interactions with pulmonary cells. Part. Fibre Toxicol 2017, 14, 42. [PubMed: 29084556]

(17). Kondej D; Sosnowski T R Effect of clay nanoparticles on model lung surfactant: a potential marker of hazard from nanoaerosol inhalation. Environ. Sci. Pollut. Res. Int 2016, 23, 4660–4669. [PubMed: 26527341]

(18). Ruge CA; Schaefer UF; Herrmann J; Kirch J; Cañadas O; Echaide M; Pérez-Gil J; Casals C; Müller R; Lehr C-M The interplay of lung surfactant proteins and lipids assimilates the macrophage clearance of nanoparticles. PLoS One 2012, 7, e40775. [PubMed: 22802970]

(19). Kapralov AA; Feng WH; Amoscato AA; Yanamala N; Balasubramanian K; Winnica DE; Kisin ER; Kotchey GP; Gou P; Sparvero LJ; Ray P; Mallampalli RK; Klein-Seetharaman J; Fadeel B; Star A; Shvedova AA; Kagan VE Adsorption of surfactant lipids by single-walled carbon nanotubes in mouse lung upon pharyngeal aspiration. ACS Nano 2012, 6, 4147–4156. [PubMed: 22463369]

(20). Konduru NV; Tyurina YY; Feng W; Basova LV; Belikova NA; Bayir H; Clark K; Rubin M; Stolz D; Vallhov H; Scheynius A; Witasp E; Fadeel B; Kichambare PD; Star A; Kisin ER; Murray AR; Shvedova AA; Kagan VE Phosphatidylserine targets single-walled carbon nanotubes to professional phagocytes in vitro and in vivo. PLoS One 2009, 4, e4398. [PubMed: 19198650]

(21). DeLoid G; Casella B; Pirela S; Filoramo R; Pyrgiotakis G; Demokritou P; Kobzik L Effects of engineered nanomaterial exposure on macrophage innate immune function. NanoImpact 2016, 2, 70–81. [PubMed: 29568809]

(22). Raesch SS; Tenzer S; Storck W; Rurainski A; Selzer D; Ruge CA; Perez-Gil J; Schaefer UF; Lehr C-M Proteomic and lipidomic analysis of nanoparticle corona upon contact with lung surfactant reveals differences in protein, but not lipid composition. ACS Nano 2015, 9, 11872–11885. [PubMed: 26575243]

(23). Mousseau F; Puisney C; Mornet S; Le Borgne R; Vacher A; Airiau M; Baeza-Squiban A; Berret J-F Supported pulmonary surfactant bilayers on silica nanoparticles: formulation, stability and impact on lung epithelial cells. Nanoscale 2017, 9, 14967–14978. [PubMed: 28953277]

(24). Kumar A; Bicer EM; Morgan AB; Pfeffer PE; Monopoli M; Dawson KA; Eriksson J; Edwards K; Lynham S; Arno M; Behndig AF; Blomberg A; Somers G; Hassall D; Dailey LA; Forbes B; Mudway IS Enrichment of immunoregulatory proteins in the biomolecular corona of nanoparticles within human respiratory tract lining fluid. Nanomed. Nanotechnol Biol. Med 2016, 12, 1033–1043.

(25). Wang F; Liu J Liposome supported metal oxide nanoparticles: interaction mechanism, light controlled content release, and intracellular delivery. Small 2014, 10, 3927–3931. [PubMed: 24861966]

(26). Demokritou P; Buchel R; Molina RM; Deloid GM; Brain JD; Pratsinis SE Development and characterization of a Versatile Engineered Nanomaterial Generation System (VENGES) suitable for toxicological studies. Inhal Toxicol. 2010, 22, 107–116. [PubMed: 20701428]

(27). Gass S; Cohen JM; Pyrgiotakis G; Sotiriou GA; Pratsinis SE; Demokritou P Safer formulation concept for flame-generated engineered nanomaterials. ACS Sustain. Chem. Eng 2013, 1, 843–857. [PubMed: 23961338]

(28). Cohen J; Deloid G; Pyrgiotakis G; Demokritou P Interactions of engineered nanomaterials in physiological media and implications for in vitro dosimetry. Nanotoxicology 2013, 7, 417–431. [PubMed: 22393878]

(29). Wohlleben W; Ma-Hock L; Boyko V; Cox G; Egenolf H; Freiberger H; Hinrichsen B; Hirth S; Landsiedel R Nanospecific guidance in REACH: A comparative physical-chemical

characterization of 15 materials with methodical correlations. J. Ceram. Sci. Tech 2013, 4, 93–104.

(30). Muller RH; Ruhl D; Luck M; Paulke B-R Influence of fluorescent labelling of polystyrene particles on phagocytic uptake, surface hydrophobicity, and plasma protein adsorption. Pharm. Res 1997, 14, 18–24. [PubMed: 9034216]

(31). Valle R P. Increasing hydrophobicity of nanoparticles Intensifiesl ung surfactant film inhibition and particle retention. ACS Sustainable Chem. Eng 2014, 2, 1574–1580.

(32). DeLoid GM; Cohen JM; Pyrgiotakis G; Demokritou P Preparation, characterization, and in vitro dosimetry of dispersed, engineered nanomaterials. Nat. Protoc 2017, 12, 355–371. [PubMed: 28102836]

(33). Folch J; Lees M; Stanley GHS A simple method for the isolation and purification of total lipides from animal tissues. J. Biol. Chem 1957, 226, 497–509. [PubMed: 13428781]

(34). Chalvardjian A; Rudnicki E Determination of lipid phosphorus in the nanomolar range. Anal. Biochem. 1970, 36, 225–226. [PubMed: 5482631]

(35). Wohlleben W; Driessen MD; Raesch S; Schaefer UF; Schulze C; von Vacano B; Vennemann A; Wiemann M; Ruge CA; Platsch H; Mues S; Ossig R; Tomm JM; Schnekenburger J; Kuhlbusch TAJ; Luch A; Lehr C-M; Haase A Influence of agglomeration and specific lung lining lipid/protein interaction on short-term inhalation toxicity. Nanotoxicology 2016, 10, 970–980. [PubMed: 26984182]

(36). Anderson TH; Min Y; Weirich KL; Zeng H; Fygenson D; Israelachvili JN Formation of supported bilayers on silica substrates. Langmuir 2009, 25, 6997–7005. [PubMed: 19354208]

(37). Michel R; Gradzielski M Experimental aspects of colloidal interactions in mixed systems of liposome and inorganic nanoparticle and their applications. Int. J. Mol. Sci. 2012, 13, 11610–11642. [PubMed: 23109874]

(38). Wassarman PM; Litscher ES Mammalian fertilization is dependent on multiple membrane fusion events. Meth. Mol. Biol 2008, 475, 99–113.

(39). Kinnunen PKJ On the molecular-level mechanisms of peripheral protein-membrane interactions induced by lipids forming inverted non-lamellar phases. Chem. Phys. Lipids 1996, 81, 151–166.

(40). Mondal Roy S; Sarkar M Membrane fusion induced by small molecules and ions. J. Lipids 2011, 2011, 528784. [PubMed: 21660306]

(41). Immordino ML; Dosio F; Cattel L Stealth liposomes: review of the basic science, rationale, and clinical applications, existing and potential. Int. J. Nanomed 2006, 1, 297–315.

(42). Jiménez-Rojo N; Lete MG; Rojas E; Gil D; Valle M; Alonso A; Moya SE; Goni FM Lipidic nanovesicles stabilize suspensions of metal oxide nanoparticles. Chem. Phys. Lipids 2015, 191, 84–90. [PubMed: 26301898]

(43). Dwivedi MV; Harishchandra RK; Koshkina O; Maskos M; Galla H-J Size influences the effect of hydrophobic nanoparticles on lung surfactant model systems. Biophys. J 2014, 106, 289–298. [PubMed: 24411261]

(44). Singh PK; Adler JJ; Rabinovich YI; Moudgil BM Investigation of Self-Assembled Surfactant Structures at the Solid–Liquid Interface Using FT-IR/ATR Langmuir 2001, 17, 468–473.

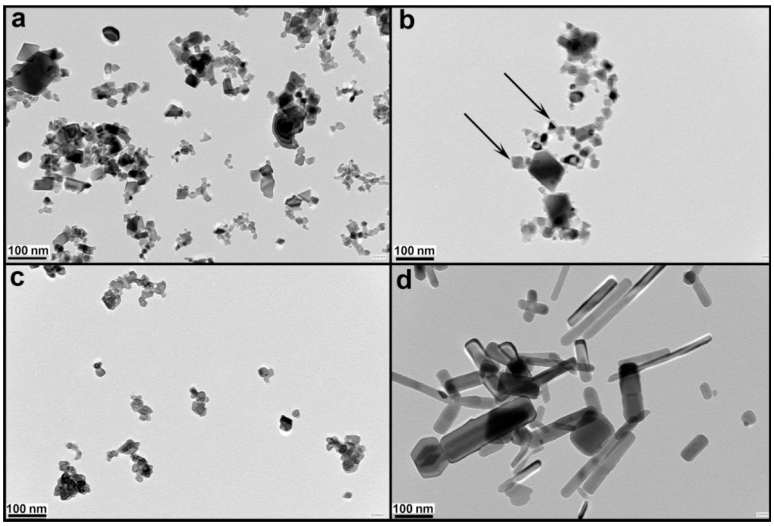

Figure 1.

Transmission electron micrographs of sonicated NP suspensions in DI water. (a) CeO_2. (b) Si-CeO_2. Nanothin coatings of amorphous silica are shown (arrows). (c) $BaSO_4$. (d) ZnO nanorods.

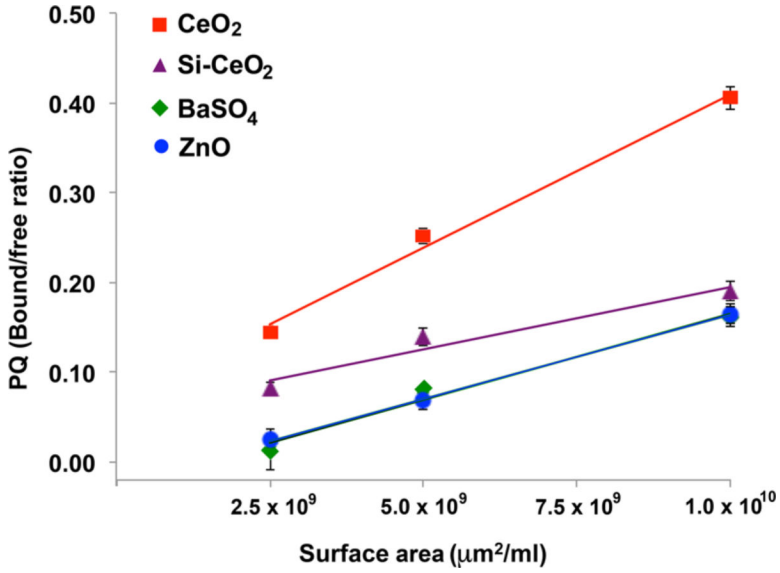

Figure 2.

Surface hydrophobicity of CeO_2, Si-CeO_2, BaSO4, and ZnO NPs determined by Rose Bengal partitioning. The relationships between NP surface areas and PQ are plotted. The data were then analyzed by performing linear regression. Following model fitting, the slopes of PQ for each NP were compared using SAS statistical software (SAS Institute, Inc. Cary, NC). The slopes of the linear regression lines are proportional to the relative hydrophobicity of NPs. The relative surface hydrophobicity was on the order of CeO_2 > ZnO = $BaSO_4$ > Si-CeO_2 NPs.

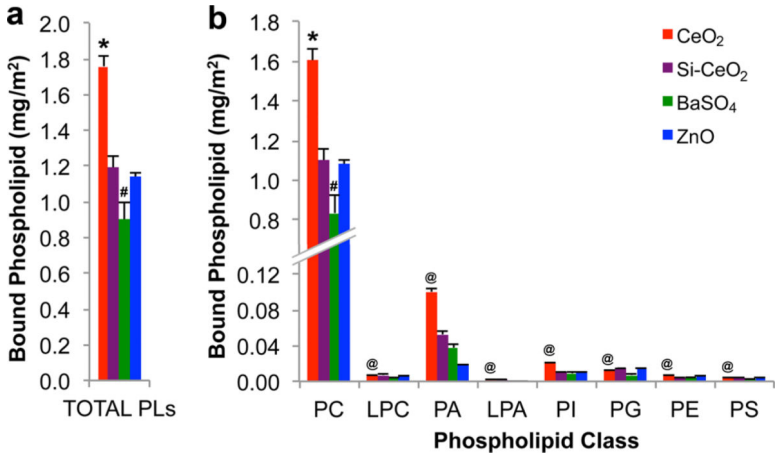

Figure 3.

Tandem quadruple mass spectroscopy analyses of lipids adsorbed on NPs after 30 min incubation in the cell-free BAL fluid. (a) Total adsorbed PLs were calculated per surface area as 1.76 ± 0.06 (CeO_2), 1.19 ± 0.06 (Si—CeO_2), 0.90 ± 0.10 ($BaSO_4$), and 1.14 ± 0.02 (ZnO) mg/m^2. (b) Amounts of different PL classes are shown. PC was the most abundant class bound to all NPs (*CeO_2 higher than the other three NPs, #BaSO4 lower than the other three NPs, MANOVA, *#P < 0.05). The amounts of NP-bound individual PL class also significantly varied among the four NP types (MANOVA, @$P < 0.05$). Data are mean ± standard deviation, $n = 3$ replicates (PC: phosphatidylcholine; LPC: lysophosphatidylcholine; PA: phosphatidic acid; LPA: lysophosphatidic acid; PI: phosphatidylinositol; PG: phosphatidylglycerol; PE: phosphatidyethanolamine; PS: phosphatidylserine).

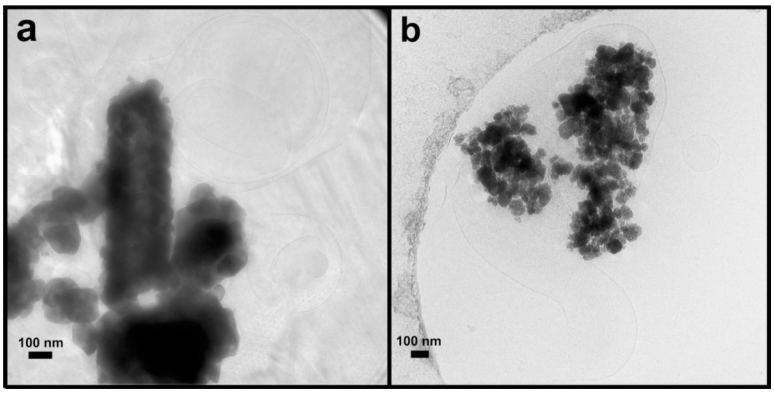

Figure 4.

Cryogenic TEM micrographs of CeO_2 and $BaSO_4$ NPs postincubation in rat BALf showing interaction of intact liposomes with agglomerates of CeO_2 (a) and $BaSO_4$ (b) NPs.

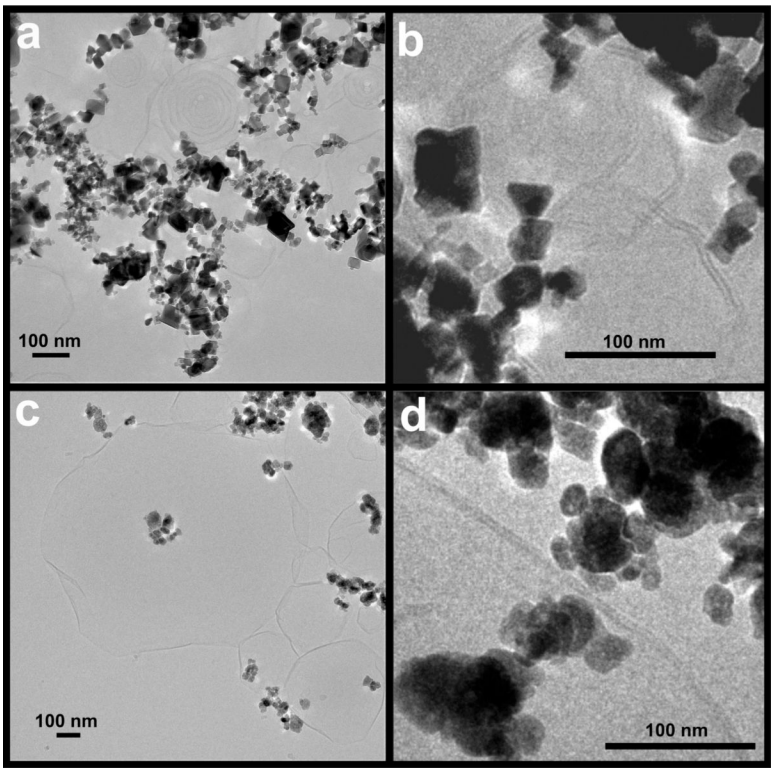

Figure 5.

Cryo-TEM micrographs of CeO_2 (a,b) and $BaSO_4$ (c,d) NPs postincubation in a 2:1 mixture of DPPC and DPPA. Multilamellar and unilamellar vesicles are seen adsorbed to clusters of CeO_2 NPs (a,b). Agglomerates of $BaSO_4$ NPs interacting with PL vesicles with polyhedral shapes (c) and lipid bilayer (d) are shown.

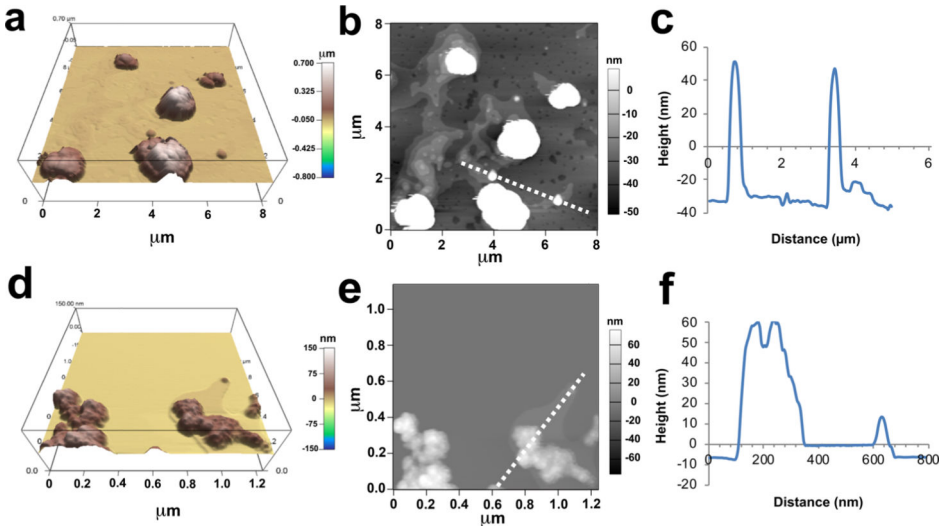

Figure 6.

Atomic force microscopy analyses of CeO_2 (a-c) and $BaSO_4$ (d-f) NP interaction with a DPPC/DPPA mixture. (a,d) Three-dimensional rendering of AFM height images. (b,e) Top view of the same images. (c,f) Height profiles across the dashed line in panels b and e.

Table 1.

Characterization of NPs Used in the Study[a]

	CeO_2	Si–CeO_2	$BaSO_4$	ZnO
SSA (m^2/g)	28.0	27.8	33.0	41.0
D_{xrd} (nm)	32.9	32.6	36.0	29.0
In Distilled Water				
D_H (nm)	136	208	144	221
ζ (mV)	34.5	−26.8	−18.50	23.00
Postincubation in BALf				
d_h (nm)	1529	460	595	2189
ζ (mV)	−23.2	−16.7	−34.5	−20.8

[a]SSA—specific surface area; D_{xrd}—diameter (based on X-ray diffraction); D_H—hydrodynamic diameter; ζ—zeta potential (ζ); BALf—bronchoalveolar lavage fluid.

Table 2.

Quantitation of PL Components Adsorbed on Different NPs after Incubation in Rat BALf[a,b]

PL	CeO2	Si-CeO_2	$BaSO_4$	ZnO
LPC	7.03 ± 0.25	7.15 ± 0.37	3.60 ± 0.38	5.69 ± 0.11
PC	1604.87 ± 57.19	1100.24 ± 56.47	834.48 ± 88.76	1079.10 ± 20.13
PE	7.03 ± 0.25	3.58 ± 0.18	4.50 ± 0.48	5.69 ± 0.11
PI	21.09 ± 0.75	9.54 ± 0.49	8.99 ± 0.96	10.24 ± 0.19
PG	12.30 ± 0.44	14.30 ± 0.73	7.19 ± 0.77	14.80 ± 0.28
PS	3.52 ± 0.13	3.58 ± 0.18	2.70 ± 0.29	3.41 ± 0.06
LPA	1.76 ± 0.06	1.19 ± 0.06	N.D.	N.D.
PA	100.19 ± 3.57	52.45 ± 2.69	37.77 ± 4.02	18.21 ± 0.34
total	1757.80 ± 62.64	1192.03 ± 61.18	899.22 ± 95.65	1138.30 ± 21.23

[a]Data are mean ± SE $\mu g/m^2$, $n = 3$ per NP.

[b]LPC—lysophosphatidylcholine; PC—phosphatidylcholine; PE—phosphatidyethanolamine; PI—phosphatidylinositol; PG—phosphatidylglycerol; PS—phosphatidylserine; LPA—lysophosphatidic acid; PA—phosphatidic acid; N.D.—not detectable.

Table 3.

Relative Abundance of PL Classes in Rat BALf and in Adsorbed Lipids on Different NPs[a,b]

		NP-associated PLs			
	rat BALf	**CeO_2**	**Si-CeO_2**	**$BaSO_4$**	**ZnO**
LPC	0.18	0.40	0.60	0.40	0.50
PC	71.59	91.30	92.30	92.80	94.80
PE	0.89	0.40	0.30	0.50	0.50
PI	2.87	1.20	0.80	1.00	0.90
PG	1.35	0.70	1.20	0.80	1.30
PS	0.53	0.20	0.30	0.30	0.30
LPA	N.D.	0.10	0.10	N.D.	N.D.
PA	0.15	5.70	4.40	4.20	1.60
SM	22.41	N.D.	N.D.	N.D.	N.D.

[a]Data are relative amounts of each PL class as % of total of all PLs measured.

[b]LPC—lysophosphatidylcholine; PC—phosphatidylcholine; PE—phosphatidyethanolamine; PI—phosphatidylinositol; PG—phosphatidylglycerol; PS—phosphatidylserine; LPA—lysophosphatidic acid; PA—phosphatidic acid; SM—sphingomyelin; BALf—bronchoalveolar lavage fluid; N.D.—not detectable.